IET Science, Measurement & Technology

Research Article

IET Journals
The Institution of Engineering and Technology

Virtual element method and permanent magnet simulations: potential and mixed formulations

ISSN 1751-8822
Received on 30th July 2020
Revised 29th September 2020
Accepted on 12th October 2020
E-First on 23rd March 2021
doi: 10.1049/iet-smt.2020.0322
www.ietdl.org

Franco Dassi[1] ✉, *Paolo Di Barba*[2], *Alessandro Russo*[1,3]

[1]*Dipartimento di Matematica e Applicazioni, Università di Milano-Bicocca, Via Cozzi 53, I-20153, Milano, Italy*
[2]*Dipartimento di Ingegneria Industriale e dell'Informazione, Via Adolfo Ferrata 1, 27100 Pavia, Italy*
[3]*IMATI-CNR, Via Ferrata 5/A, 27100 Pavia, Italy*
✉ *E-mail: franco.dassi@unimib.it*

Abstract: The methodological background of the virtual element method is presented and applied to model permanent magnets via the Kikuchi formulation, considering both linear and non-linear magnetic permeability of the ferromagnetic regions. The authors examine several study cases: a permanent magnet in free space, a permanent magnet energising a ferromagnetic core, a four-pole permanent-magnet motor. In order to validate the proposed approach, comparisons with both virtual and finite element potential formulations are presented and discussed.

1 Introduction

The virtual element method (VEM) is a recent generalisation of classical finite elements allowing for very general domain decompositions (polygons and polyhedra [1], even with curved edges/faces [2, 3]) and approximation spaces enjoying features difficult to obtain in the classical setting [4] (e.g. truly divergence-free vector functions [5, 6]). Other important features of VEM are:

- the possibility of using hanging nodes in the decomposition without special treatments [7];
- the compatibility with finite element method (FEM), meaning that VEM and FEM can both be used at the same time;
- excellent robustness with respect to degeneracies of the mesh (polygons/polyhedra with small edges/faces) [8, 9];
- sound mathematical analysis [10].

In this paper, we apply the VEM to the discretisation of classical magnetostatics problems, including the modelisation of permanent magnets, to validate this new methodology and emphasise the advantages over the classical finite element techniques.

As far as case studies are concerned, it is difficult to overlook the technological importance of permanent magnets as core components of modern electrical devices like small-size motors for domestic appliances or traction motors for full-electric vehicles. Accordingly, for a permanent magnet to be a valid and competitive industrial product, designers need advanced tools for accurate field modelling; this is the basic rationale inspiring the application of VEM in magnetics here presented.

The remaining part of this paper is organised as follows. In Section 2, we present the continuous formulation of a magnetostatic problem in the Kikuchi mixed form. We introduce the VEM used to solve such kind of problem in Section 3. Then, in Section 4, we present the VEM discrete counterpart of the magnetostatic Kikuchi mixed problem. In Section 5, we show some numerical examples. First, we simulate a permanent magnet surrounded by air and iron. Then, we consider a magnetic circuit energised by a permanent magnet both in a linear and a non-linear framework. Finally, we make a simulation of an interior-permanent-magnet motor. In such examples, special emphasis is given to VEM discretisation techniques of two-dimensional (2D) domains (general polygons, hanging nodes), as well as the use of polynomial projectors for post-processing computation of field-related quantities like forces and torques.

2 Kikuchi formulation of 2D magnetostatics

In this paper, we consider the mixed formulation proposed by Kikuchi in [11]: find the pair $(\boldsymbol{H}, p)$ solution of

$$\begin{cases} \displaystyle\int_\Omega \mathrm{rot}\,\boldsymbol{H}\,\mathrm{rot}\,\boldsymbol{v}\,\mathrm{d}\Omega + \int_\Omega \nabla p\cdot\mu\boldsymbol{v}\,\mathrm{d}\Omega = \int_\Omega j\,\mathrm{rot}\,\boldsymbol{v}\,\mathrm{d}\Omega \\ \displaystyle\int_\Omega \nabla q\cdot\mu\boldsymbol{H}\,\mathrm{d}\Omega = 0 \end{cases} \tag{1}$$

where since we are considering an isotropic material, $\mu = \mu_0\mu_r$ is the scalar magnetic permeability obtained by the product between the magnetic permeability of the vacuum, μ_0, and the relative permeability, μ_r, $\boldsymbol{H}$ is the magnetic field, p plays the role of a Lagrange multiplier to enforce weakly the condition $\mathrm{div}\,\boldsymbol{B} = 0$ and the functions $\boldsymbol{v}$ and q are proper test functions.

In the presence of a permanent magnet, the induction field $\boldsymbol{B}$ is decomposed in the following form:

$$\boldsymbol{B} = \mu\boldsymbol{H} + \boldsymbol{B}_0, \tag{2}$$

where $\boldsymbol{B}_0$ is the induction field due to the magnet. Now the divergence-free condition on $\boldsymbol{B}$ becomes

$$\mathrm{div}(\boldsymbol{B}) = \mathrm{div}(\mu\boldsymbol{H} + \boldsymbol{B}_0) = 0. \tag{3}$$

Consequently, when we are considering the presence of a permanent magnet the second condition of (1) has to be substituted by

$$\int_\Omega \nabla q\cdot\mu\boldsymbol{H}\,\mathrm{d}\Omega = -\int_\Omega \nabla q\cdot\boldsymbol{B}_0\,\mathrm{d}\Omega,$$

which is the weak form of the strong condition defined in (3).

In the numerical examples, we compared the proposed model with a standard potential formulation where the permanent magnet is approximated via equivalent current sheets [12]. In such cases, we consider both the virtual element formulation proposed in [13] and the classical finite element one [14]. To get the numerical solution of such finite element approximation, we use the commercial code MagNet [15].

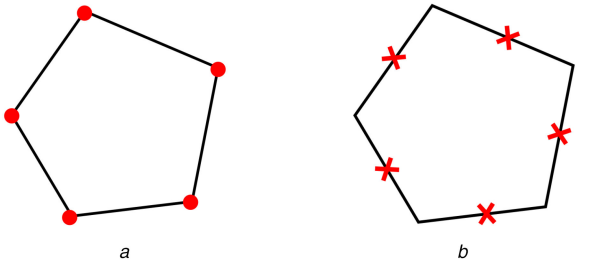

Fig. 1 *VEM dofs for a pentagon in the lowest-order*
(a) Scalar variable p_h, ***(b)*** Vectorial variable $\boldsymbol{H}_h$ for. All the dofs are functions evaluations

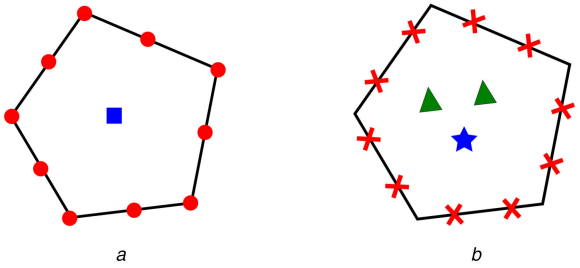

Fig. 2 *VEM dofs for a pentagon degree 2*
(a) Scalar variable p_h, ***(b)*** Vectorial variable $\boldsymbol{H}_h$. In a virtual element framework, dofs can be the evaluation of function (dots and cross) and moments (triangles, squares and stars) [13]

3 Virtual element functions

To better understand the virtual element discretisation of the problem (1), we focus on the description of the approximation spaces involved. First, we consider the lowest-order case, $k = 1$, then we show how to extend it for a generic approximation degree k. In the last subsection, we have made some key considerations about virtual functions from both a theoretical and practical point of view.

Given a domain $\mathcal{D}$, we define $\mathbb{P}_k(\mathcal{D})$ as the space of polynomials of degree up to k defined in $\mathcal{D}$. In such a framework $\mathcal{D}$ can be an edge e or a polygon E.

Consider a discretisation Ω_h of the computational domain made of polygons. In the following paragraphs, we present the lowest-order and general-order cases. For a more detailed description of them, we refer to [13].

3.1 Lowest-order case ($\boldsymbol{k} = 1$)

The scalar variable p is approximated by a function p_h linear on each edge and harmonic inside each element, i.e.

$$p_h|_e \in \mathbb{P}_1(e) \quad \text{and} \quad \Delta p_h = 0 \ \text{ in } E,$$

where e and E are a generic edge and element of the mesh Ω_h, respectively. In such a case, the degrees of freedom (dofs) of p_h are the values of p_h at polygon vertexes, as shown in Fig. 1*a*.

The magnetic field $\boldsymbol{H}$ is approximated by a discrete vector function $\boldsymbol{H}_h$ characterised by the constant rotor, zero divergence and whose tangential component is constant on each edge e of Ω_h:

$$\boldsymbol{H}_h \cdot \boldsymbol{t}_e|_e \in \mathbb{P}_0(e), \quad \operatorname{div} \boldsymbol{H}_h = 0 \text{ in } E \text{ and } \operatorname{rot} \boldsymbol{H}_h \in \mathbb{P}_0(E),$$

where $\boldsymbol{t}_e$ is the tangential vector of an edge e. For such vectorial function, the dofs are the tangential component value on each edge, as shown in Fig. 1*b*.

3.2 General-order case

For $k \geq 2$, the Lagrange multiplier variable p_h is defined by the conditions

$$p_h|_e \in \mathbb{P}_k(e) \quad \text{and} \quad \Delta p_h \in \mathbb{P}_{k-2}(E).$$

In such a general-order case, p_h is uniquely identified by

- the nodal values of p_h at each polygon vertex;
- $k - 1$ values of p_h on each polygon edge;
- the moments

$$\int_E (\nabla p_h \cdot \boldsymbol{x}) p_{k-2} \mathrm{d}E \quad \forall p_{k-2} \in \mathbb{P}_{k-2}(E),$$

where $\boldsymbol{x} := (x, y)^t$.

Since in the numerical experiments of Section 5, we use degree $k = 2$, we show the scheme of such dofs in Fig. 2*a*.

The approximated magnetic field $\boldsymbol{H}_h$ is defined by

$$\boldsymbol{H}_h \cdot \boldsymbol{t}|_e \in \mathbb{P}_{k-1}(e), \ \operatorname{div} \boldsymbol{H}_h \in \mathbb{P}_{k-2}(E), \operatorname{rot} \boldsymbol{H}_h \in \mathbb{P}_{k-1}(E). \quad (4)$$

In this case, the dofs are

- $k - 1$ values of $\boldsymbol{H}_h \cdot \boldsymbol{t}_e$ for each polygon edge e;
- the moments

$$\int_E (\boldsymbol{H}_h \cdot \boldsymbol{p}) p_{k-2} \mathrm{d}E, \quad p_{k-2} \in \mathbb{P}_{k-2}(E),$$

the moments of the rotor

$$\int_E \operatorname{rot} \boldsymbol{H}_h p^0_{k-1} \mathrm{d}E, \quad p^0_{k-1} \in \mathbb{P}_{k-1}(E) \setminus \mathbb{P}_0(E).$$

In Fig. 2*b*, we give the scheme of the dofs for $\boldsymbol{H}_h$ considering the case $k = 2$.

3.3 Global spaces

The global spaces for $\boldsymbol{H}_h$ and p_h are obtained by gluing such local spaces along edges. As a result p_h will be globally continuous, while only the tangential component of $\boldsymbol{H}_h$ will be continuous across edges. Then, the dofs of such global spaces are the union of the local ones. We refer to such spaces as $\boldsymbol{V}_h$ and Q_h for the field and the multiplier variables, respectively.

If we consider the lowest-order case and a mesh Ω_h made of triangles, the vector space $\boldsymbol{V}_h$ coincides with the classical FEM edge space described in [16–18], while the space Q_h is simply the linear Lagrange FEM space [19].

To solve a magnetostatic problem one can consider a potential formulation [4, 13]. This formulation has fewer dofs than the Kikuchi formulation. Indeed, given a mesh made of triangles with N_V vertexes, we roughly have $k^2 N_V$ and $3k^2 N_V$ dofs for potential and Kikuchi formulations, respectively. However, the increased computational effort of the Kikuchi approximation results in a much more robust method with respect to singularities due to re-entrant corners and discontinuities of the permeability μ.

3.4 Important considerations on virtual functions

Functions $\boldsymbol{H}_h$ and p_h are virtual so we know them *only* through the values of their dofs.

Consequently, in principle, one has to compute such virtual functions to get direct access to them. Indeed, given a polygon E of the mesh, one could in principle define an auxiliary PDE having the virtual function as unknown, sub-triangulate E, and get a numerical solution that approximates the virtual function at hand inside E. However, this strategy is against the main idea of VEM!

Indeed, starting from the dofs, it is possible to compute some quantities in a straightforward way without solving any auxiliary partial differential equation (PDE).

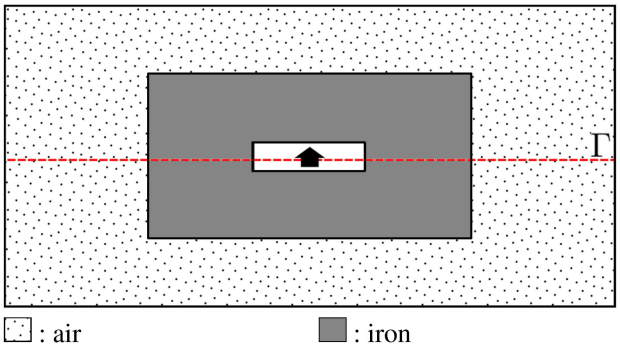

Fig. 3 *Permanent magnet: the configuration with the iron. We highlight the path* Γ *where we evaluate the* $\mathbf{y}$*-component of the magnetic fields* $\boldsymbol{B}$ *and* $\boldsymbol{H}$

First of all, we can find the polynomial that represents the rotor of $\boldsymbol{H}_h$ in E. Then, we can define the L^2 projection operator on each mesh element E. Such projection operator maps the virtual function $\boldsymbol{H}_h$ restricted to the element E into the space of vectorial polynomials of degree $k-1$. We recall that the definition of such projection is based on the following identity:

$$(\Pi_{k-1}\boldsymbol{H}_h, \boldsymbol{p}) = (\boldsymbol{H}_h, \boldsymbol{p}) \quad \text{for all } \boldsymbol{p} \in [\mathbb{P}_{k-1}(E)]^2, \tag{5}$$

where $(\cdot\,,\cdot)$ is the standard L^2 inner product [13]. In a similar way, it is possible to define a suitable L^2 projection operator for the scalar variable p_h [4].

Both rot $\boldsymbol{H}_h$ and the projection operators play a key role in the virtual element formulation. Indeed, they are exploited to discretise problem (1). More specifically, they are used to build the discrete bilinear forms of problem (1).

The projection operator (5) is also instrumental in a post-processing procedure. In Section 5, we will give numerical evidence about this fact in a real-life example. Indeed, we will use $\Pi_{k-1}\boldsymbol{H}_h$ to get an approximation of the magnetic field and to compute some derived quantities such as the energy of the vector field or Maxwell stress tensor [14, 20].

We make a further remark about the correct use of the constitutive law of a permanent magnet in the VEM formulations taken into account. For a $\boldsymbol{B}$-oriented formulation, like the potential formulation, one obtains $\boldsymbol{B}$ as the curl of vector potential (in 3D domains) or as the rotated gradient of a scalar potential in 2D; therefore, $\boldsymbol{H}$-field inside the permanent magnet is given by

$$\boldsymbol{H} = (\mu_0\mu_r)^{-1}(\boldsymbol{B} - \boldsymbol{B}_0)\,.$$

On the contrary, for an $\boldsymbol{H}$-oriented formulation, like the Kikuchi-like formulation, one obtains $\boldsymbol{H}$ as the native unknown; therefore, $\boldsymbol{B}$-field inside the permanent magnet is given by (2).

4 Discretisation of the problem

Once the spaces $\boldsymbol{V}_h$ and Q_h are constructed, the discretisation of the problem follows the variational approach as in FEM: find $(\boldsymbol{H}_h,\ p_h) \in \boldsymbol{V}_h \times Q_h$ such that

$$\begin{cases} \displaystyle\int_{\Omega_h} \operatorname{rot}\boldsymbol{H}_h \operatorname{rot}\boldsymbol{v}_h\,\mathrm{d}\Omega + [\nabla p_h, \mu\boldsymbol{v}_h]_e = \int_{\Omega_h} j \operatorname{rot}\boldsymbol{v}_h\,\mathrm{d}\Omega \\ [\nabla q_h,\ \mu\boldsymbol{H}_h]_e = [\nabla q_h,\ \boldsymbol{B}_0]_{\mathrm{pm}} \end{cases} \tag{6}$$

where $\boldsymbol{v}_h \in \boldsymbol{V}_h$ and $q_h \in Q_h$ are test functions

$$[\nabla p_h, \mu\boldsymbol{v}_h]_e \simeq \int_\Omega \nabla p \cdot \mu\boldsymbol{v}\,\mathrm{d}\Omega,$$

and

$$[\nabla q_h, \boldsymbol{B}_0]_{\mathrm{pm}} \simeq -\int_\Omega \nabla q \cdot \boldsymbol{B}_0 \mathrm{d}\Omega\,.$$

These last two bilinear forms are built starting from the dofs and the projection operator defined in (5). We refer to Subsection 3.3 in [13] for a detailed description and analysis of them.

If we are able to integrate polynomials on generic polygons, some of the integrals in (6) are computed 'exactly', i.e. up to quadrature approximation rule precision. Indeed, given a function $\boldsymbol{v}_h \in \boldsymbol{V}_h$, rot $\boldsymbol{v}_h$ is a polynomial that can be computed starting from the dofs of $\boldsymbol{v}_h$. Consequently, the first integral which involves only rotor of functions in $\boldsymbol{V}_h$ is exact, if we choose a proper quadrature rule precision degree. Similar considerations can be done on the integral appearing at the right-hand side of the first equation in (6), but we have to take into account the approximation of the current density j.

In the last two numerical experiments of Section 5, we consider a non-linear approximation of the magnetic permeability μ_r. To achieve this goal, we consider a fixed-point iterative scheme. More specifically, given the discrete magnetic field $\boldsymbol{H}_h^i$ at the ith iteration and the constitutive law $\mu_r\colon \mathbb{R}^+ \to \mathbb{R}^+$, since $\boldsymbol{H}_h^i$ is virtual and we cannot compute the $\|\boldsymbol{H}_h^i\|$, we exploit the projection operator to get the value of μ_r at the quadrature points, i.e. $\mu_r\big(\|\Pi_{k-1}\boldsymbol{H}_h^i\|\big)$. Then, such values are used to compute the solution of the next iteration, i.e. $\boldsymbol{H}_h^{i+1}$. We break such iterative procedure when two subsequent solutions are close to each other, i.e. when the solution vectors are close to each other

$$\frac{\left\|\mathrm{Dof}\left(\boldsymbol{H}_h^{i+1}\right) - \mathrm{Dof}\left(\boldsymbol{H}_h^{i}\right)\right\|}{\left\|\mathrm{Dof}\left(\boldsymbol{H}_h^{i}\right)\right\|} < \epsilon,$$

where ϵ is a proper tolerance value and $\mathrm{Dof}(\cdot)$ is the operator which associates the vector of the dofs with the discrete virtual solutions, $\boldsymbol{H}_h^{i+1}$ and $\boldsymbol{H}_h^i$.

5 Numerical examples

In this section, we consider three problems that involve permanent magnets. The aim is to numerically validate VEM from the post-processing point of view. In each example, we refer to the Kikuchi mixed formulation as Kik, to the virtual element potential formulation as Pot and to the commercial code MagNet [15] as Mag. In some tests, to validate both Kikuchi and potential VEM formulations, we will consider the results provided by MagNet as a reference solution.

5.1 Permanent magnet

In this case, we consider a rectangular permanent magnet of dimension 20 mm × 80 mm, we set $\mu_r = 1$ and $\boldsymbol{B}_0 = 1$ T. We take into account two configurations. The first one where the magnet is only surrounded by air and the second one where there is iron ($\mu_r = 1000$) and air around it, as shown in Fig. 3.

The aim of this example is to verify that both fields $\boldsymbol{B}$ and $\boldsymbol{H}$ obtained by VEM approaches are in accordance with those provided by MagNet. Magnet is based on FEM, it cannot handle

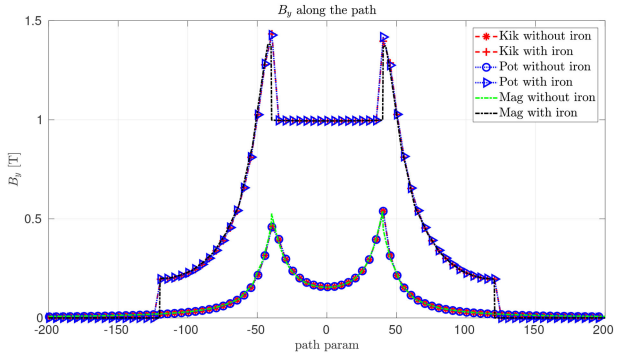

Fig. 4 *Permanent magnet: **y**-component of the field **B** along* Γ. *We show the results with and without iron*

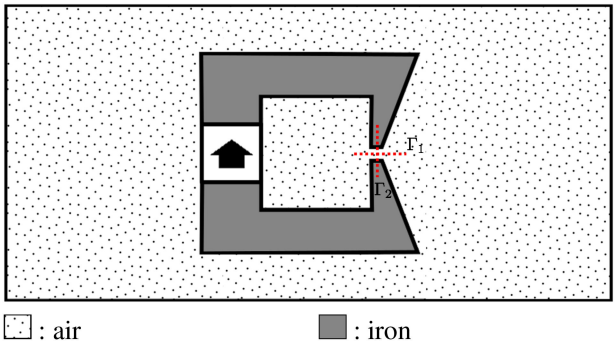

Fig. 5 *Permanent magnet circuit: the configuration taken into account. We highlight the paths* Γ_1 *and* Γ_2, *where we compute* $\boldsymbol{B}_y$

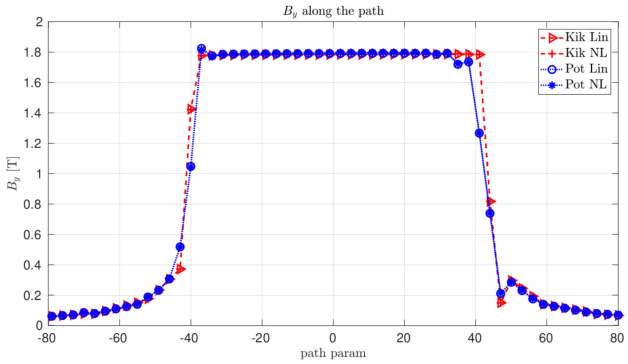

Fig. 6 *Permanent magnet circuit: values of* $\boldsymbol{B}_y$ *along the path* Γ_1

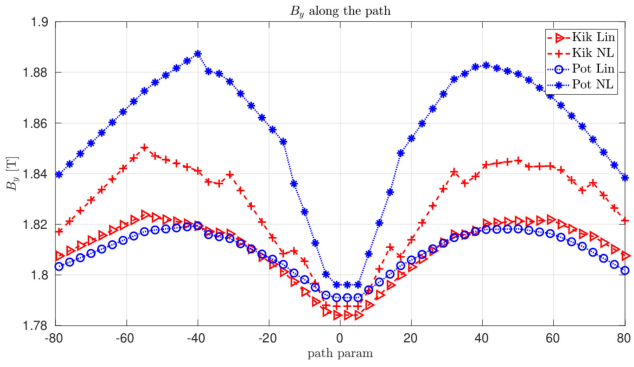

Fig. 7 *Permanent magnet circuit: values of* $\boldsymbol{B}_y$ *along the path* Γ_2. *Please note that the highest discrepancy between such curves is ∼3% so all the simulations provide similar results*

polygonal meshes so we discretise the computational domain with an unstructured quasi-uniform triangular mesh.

We compare $\boldsymbol{B}$ and $\boldsymbol{H}$ along the path Γ depicted in Fig. 3. Since the magnet is oriented in the up direction, we compare only the y-component of such fields due to the fact that the x-component is close to zero for both $\boldsymbol{B}$ and $\boldsymbol{H}$.

In Fig. 4, we show the results for each configuration taken into account, i.e. the y-component of $\boldsymbol{B}$ with and without the iron. The results obtained by both VEM approaches are in accordance with that obtained by MagNet. We got a similar agreement for the $\boldsymbol{H}$ field too, but we do not show it.

We further underline that when we consider the virtual element approaches, we exploit the projection operator, (5), to compute the vector fields $\boldsymbol{B}$ and $\boldsymbol{H}$. Consequently, such a projection operator offers a good numerical approximation of the magnetic field itself and it can be used in a post-processing framework.

Starting from this consideration, we can infer that all the derived quantities, such as the energy of the vector field or Maxwell stress tensor, can be properly computed via such a projection operator. In the next subsection, we will give numerical evidence about this fact.

5.2 Permanent magnet circuit

In this example, we consider a rectangular permanent magnet of dimension 50 mm × 50 mm energising a C-shaped magnetic circuit, characterised by a non-uniform section, as shown in Fig. 5. We set $\mu_r = 1$, $\boldsymbol{B}_0 = 1\,\mathrm{T}$ for the magnet and we take a varying air-gap d from 1 to 4 mm with a step-size of 0.5 mm, while we fix the air-gap width to 2 mm, as shown in Fig. 5. We consider both linear and non-linear approximation of the magnetic permeability of the iron core. In the former case, we take $\mu_r = 1000$, while we use the function $\mu(\boldsymbol{H})$ of iron 0.5 mm proposed in [21]. We compute the magnetic energy of different regions and in the whole domain varying the air-gap d. Moreover, we numerically verify the energy conservation law in the linear case.

The goal of such example is two-fold. On the one hand, we validate the proposed non-linear approach by showing that it gives similar results to the ones obtained via a linear approximation. This fact is aligned with the physics of the problem at hand; indeed it means that the magnetic field inside the iron is not so strong to saturate the iron inside.

On the other hand, we give numerical evidence that the projection operators are suitable to compute some derived quantities. More specifically, to compute the energy on a specific region D, we use the standard formula

$$W = \frac{1}{2}\int_D \boldsymbol{B}\cdot\boldsymbol{H}\,\mathrm{d}D$$

where we substitute both fields $\boldsymbol{B}$ and $\boldsymbol{H}$ with their VEM projection counterpart.

In Figs. 6 and 7, we provide the values of $\boldsymbol{B}_y$ when we consider an air-gap equal to 1.0 mm. The simulations obtained via either linear or non-linear case give reasonable results, since they are approximately the same and lower than 2 T. We get similar results (not shown here) for larger air-gaps. Indeed, the linear and non-linear cases are in accordance for both Kikuchi and potential VEM formulations.

Now we move to the computation of the energy. Let E_{Pot} and E_{Kik} be the energies associated with the potential and Kikuchi VEM formulation, respectively. First of all, we numerically verify that $E_{\mathrm{Pot}} \simeq E_{\mathrm{Kik}}$. To achieve this goal, we compute

$$\delta_E := \frac{|E_{\mathrm{Pot}} - E_{\mathrm{Kik}}|}{E_{\mathrm{Kik}}},$$

and the close to zero δ_E is, the more such formulations are in accordance with the energy inside the air-gap.

In Tables 1 and 2, we collect the results obtained by varying air-gap for the linear and non-linear cases. All the values of δ_E are small enough so we infer that the computation provided by both virtual element methods is in accordance with each other. Moreover, since the values of Table 1 are close to the corresponding ones in Table 2, we deduce that the linear

Table 1 Permanent magnet circuit: values of the energy obtained by varying the air-gap in the linear case

Air-gap, mm	1.0	1.5	2.0	2.5	3.0	3.5	4.0
E_{Pot}, J	25.51	30.95	34.19	36.16	37.35	38.18	38.33
E_{Kik}, J	25.31	30.60	33.94	36.14	37.40	38.00	38.51
δ_E	0.0080	0.0115	0.0073	0.0006	0.0012	0.0047	0.0047

Table 2 Permanent magnet circuit: values of the energy obtained by varying the air-gap in the non-linear case

Air-gap, mm	1.0	1.5	2.0	2.5	3.0	3.5	4.0
E_{Pot}, J	25.59	31.26	34.69	36.81	38.12	38.84	39.22
E_{Kik}, J	25.39	30.77	34.20	36.47	37.78	38.60	38.96
δ_E	0.0078	0.0159	0.0141	0.0093	0.0090	0.0062	0.0066

Table 3 Permanent magnet circuit: values of δ_C in the linear case with both Kikuchi and potential formulations

Air-gap, mm	1.0	1.5	2.0	2.5	3.0	3.5	4.0
Kikδ_C	0.0119	0.0162	0.0153	0.0122	0.0122	0.0098	0.0110
Potδ_C	0.0008	0.0012	0.0013	0.0012	0.0014	0.0012	0.0015

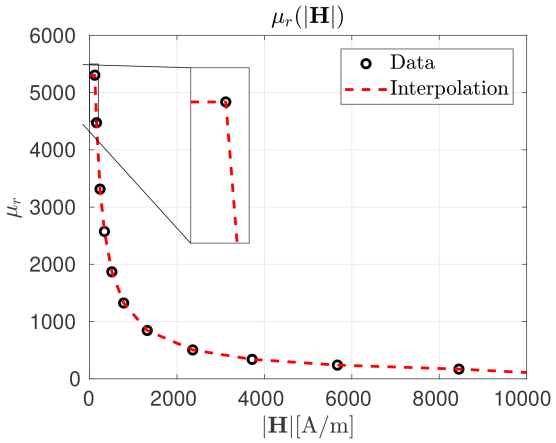

Fig. 8 *Permanent magnet motor: $\mu_r - \boldsymbol{H}$ curve used*

approximation of μ_r is still valid from the physical point of view for all air-gaps taken into account.

In such example, the energy of the whole system is due to the magnet. As a consequence, the sum of the energies inside iron and air has to be equal to the energy of the magnet, i.e.

$$E_{\text{Air}} + E_{\text{Iron}} = E_{\text{Magnet}}\,. \tag{7}$$

We consider only the linear case and we numerically verify that the identity of (7) holds. We have taken into account the linear case since the computation of the energy is more straightforward and it is not effected by how we approximate the non-linear function $\mu(\boldsymbol{H})$.

To verify the conservation of energy, we proceed in a similar way as before. We define the quantity

$$\delta_C = \frac{\left|E_{\text{Air}} + E_{\text{Iron}} - E_{\text{Magnet}}\right|}{E_{\text{Magnet}}},$$

the closer to zero this quantity is, the more the energy of the system is preserved.

In Table 3, we report the value of δ_C obtained by varying the air-gap with both VEM formulations. Such values are close to zero so we have a good agreement with (7). Moreover, we observe that the potential VEM formulation gains one order with respect to the Kukuchi one. Indeed, the discrepancy, in this case, is about 1%, while in the potential formulation is 0.1%.

5.3 Permanent magnet motor

An internal-permanent-magnet motor characterised by 4 poles and 12 stator slots is considered as a further case study. The external and the rotor diameters are 68 and 30 mm, respectively, while the air-gap width is 0.5 mm. The permanent magnet exhibits a radial magnetisation with a remanent field equal to $\boldsymbol{B}_0 = 1$ T and coercive field equal to $\boldsymbol{H}_c = 7.957e + 05\,\text{Am}^{-1}$. The $\mu_r - \boldsymbol{H}$ curve featuring the laminated magnetic core of the rotor and stator is shown in Fig. 8. The saturation effect is likely to appear inside the small magnetic bridges located in the rotor region between adjacent magnets [21].

From a physical point of view, we validate the proposed virtual element method in the computation of the cogging torque, i.e. the torque acting on the rotor when the three-phase current in the rotor slots is zero (no-load operation). Such quantity is important to design a permanent magnet motor since it takes into account the tendency of the permanent magnet axis to align with the direction that corresponds to the minimum energy stored in the motor. Although its value is substantially lower than the running torque due to the on-load current, cogging torque could be responsible for annoying vibrations occurring during the normal on-load operation of the motor.

However, before dealing with such computations, we would like to underline the advantages provided by VEM from the mesh generation point of view.

As can be seen from Fig. 9, the computational domain is complicated. Moreover, since we are considering different angular positions of the rotor, one has to generate one mesh for each rotor position. However, thanks to the virtual element method, one can avoid this time-consuming operation, exploiting polygons and the possibility to add hanging-nodes.

Before going into the detail of the adopted meshing procedure, we underline that one can consider hanging nodes in a finite element framework too, but this extension brings more complexity from the theoretical and implementation point of view [22, 23]. On the contrary, in VEM hanging nodes are *simply* two consecutive edges that lie on the same line, and they do not need any special treatment. Consider a square with a hanging node on one edge, as shown in Fig. 10*a*. In a virtual element framework, such an element is a (degenerate) pentagon. Consequently, if a code is able to deal with a pentagon, it is able to manage a square with a hanging node too: there is no need for interpolations or handling particular configurations/cases as in [22]. Moreover, we can put as many hanging nodes as we need and they can be arbitrarily placed inside the edge *without* any further issue see Fig. 10*b*.

Such flexibility can be exploited to glue meshes together and, as one can see from the description of the following mesh generation procedure, this is the main feature of VEM we exploit to discretise the motor represented in Fig. 9.

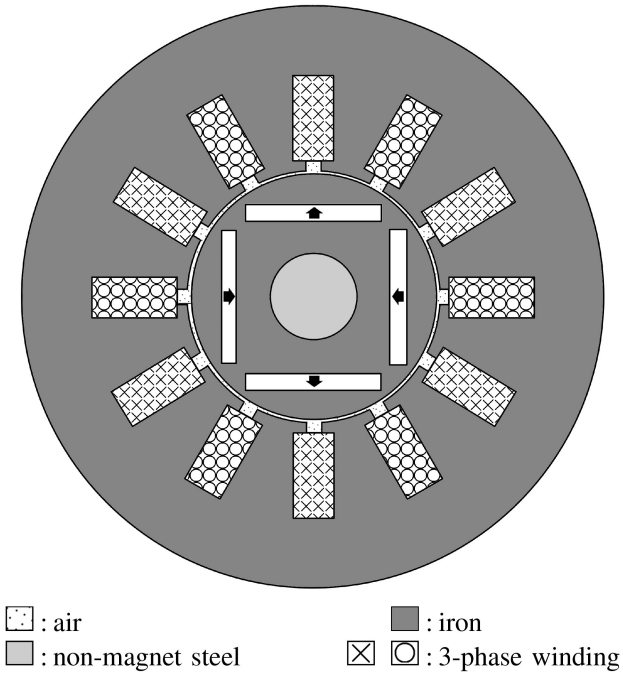

Fig. 9 *Permanent magnet motor: the geometry of the 4-pole motor taken into account*

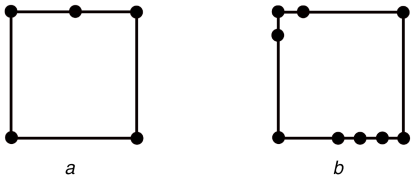

Fig. 10 *Permanent magnet motor: two squares*
(a) Degenerate pentagon, ***(b)*** Degenerate decagon

First, we generate the mesh of each subdomain separately, see Fig. 11*a*, and then we merge together with each sub-domains. At this step, we get two meshes: one discretises the stator region and the other the rotor region of the permanent magnet motor, respectively, as shown in Fig. 11*b*. To generate the final mesh, we rotate the rotor mesh by an arbitrary angle, and finally, we glue the stator and rotor meshes together, as shown in Fig. 11*c*.

We underline some advantages from the mesh generation point of view.

First of all, we can split the meshing procedure on each component and exploit different strategies according to the shape of the domain we are considering. In this example, slots and magnets can be meshed by standard structured quadrilateral meshes. The complex geometries of the iron parts of the rotor and the stator can mesh via triangles. Finally, the air-gap region is meshed by a sequence of quadrilaterals with hanging nodes to fit the curved geometry, as shown in Fig. 11*a*.

Then, one can exploit symmetries of the domain to generate *only* one mesh for different parts. In this particular case, we generate only two meshes for the magnet and the slot. The other meshes are obtained by translation and rotation of these two ones.

Moreover, the standard finite element code allows for gluing procedure of step (c) between triangular meshes. Since they are not able to handle hanging nodes, such gluing procedure is done node-by-node so the rotation is constrained to specific angles which depends on the discretisation itself, as shown in Fig. 12. The proposed meshing procedure does not have such limitations. Indeed, we can rotate the rotor mesh with an arbitrary angle and glue it with stator mesh by adding as many hanging nodes as we need.

Now we proceed with the computation of the cogging torque. The accurate field models provided by the projection operators of both Kikuchi and potential formulations allow us to compute the torque. In Fig. 13, we show the induction map for a specific angle,

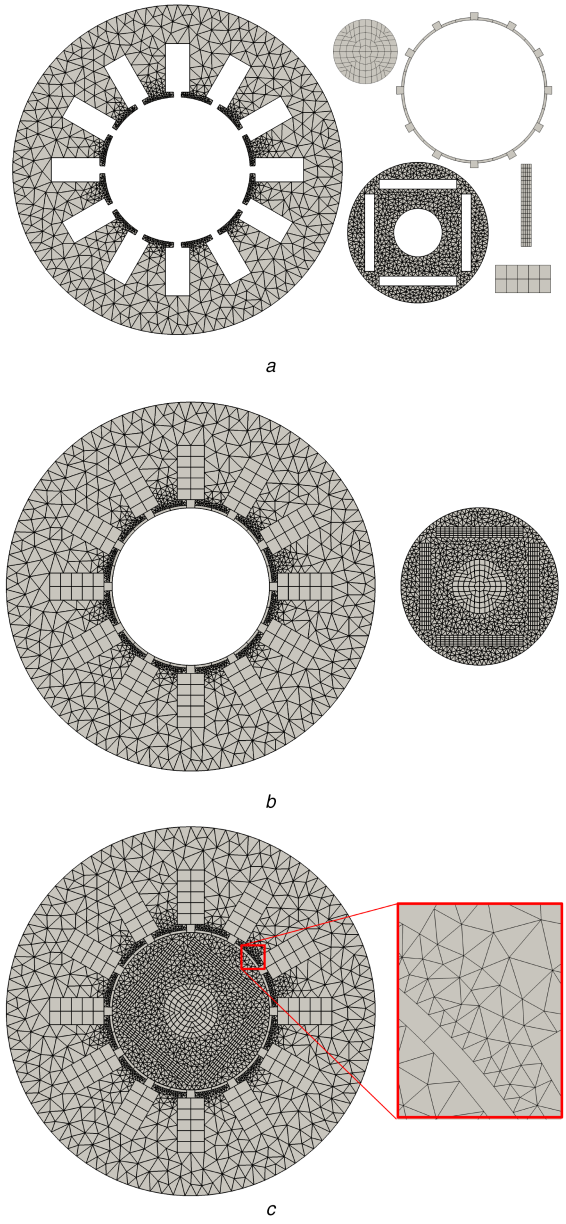

Fig. 11 *Permanent magnet motor: steps to generate the mesh of the permanent magnet motor*
(a) All the pieces of the computational domain, ***(b)*** The pieces are assembled to get the rotor and stator meshes, respectively, ***(c)*** Rotor and stator mesh are glued together and a detail of the connected boundary

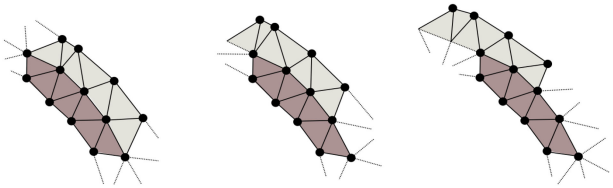

Fig. 12 *Permanent magnet motor: a way to move the mesh node-by-node in a standard finite element framework*

21°, when the motor current is zero obtained with the Kikuchi formulation, a similar map holds for the potential formulation.

To compute such quantity, we use the Maxwell stress tensor approach considering a cylindrical surface co-axially located with respect to the rotation axis as the integration surface accordingly. In Fig. 14, we show the torque-angle curve for step equal to 1°. As expected, the torque period is equal to 30°, indeed

$$360°/\mathrm{LCM}(4, 12) = 30°,$$

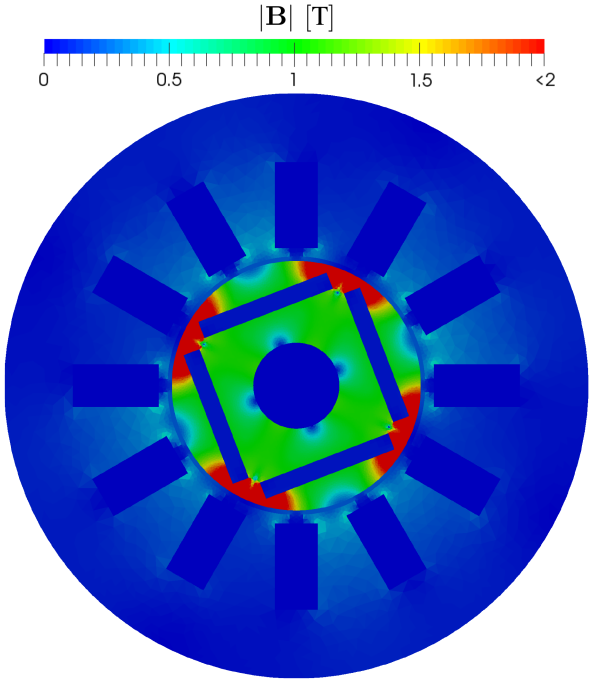

Fig. 13 *Permanent magnet motor: magnetic induction map with an angle of* 21°

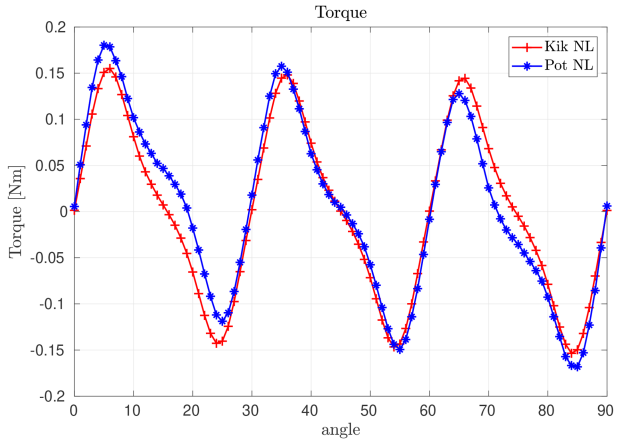

Fig. 14 *Permanent magnet motor: values of torque for different position of the rotor*

where LCM is the least common multiple operator and 4 and 12 are the number of permanent magnets and slots, respectively. Moreover, it exhibits zero mean value over the period. Once again, there is a good agreement between Kikuchi and potential virtual element formulations.

6 Conclusion

In this paper, we provide a VEM to simulate permanent magnets. To solve such problems, we focus on the VEM approximation of the Kikuchi formulation, but we compare the results with both the VEM and FEM approximation of the vector potential formulation. In particular, we propose a new way to model permanent magnets within Kikuchi formulation in contrast to the standard current sheet model of the potential approach.

We test the flexibility in mesh generation of VEM for a complex computational domain: the permanent magnet motor. We observe that the presence of many hanging nodes and arbitrarily shaped polygons do not affect the numerical results.

We further underline that such flexibility can be exploited by combining virtual and finite element approaches. Indeed, one can use virtual element spaces and functions over elements characterised by hanging nodes and polygonal elements while standard finite elements over triangles and squares.

The fields $\boldsymbol{B}$ and $\boldsymbol{H}$ are approximated by such projection operators and they are also exploited to compute some derived quantities. Indeed, we numerically prove that energy, Maxwell stress tensor and torque computed via the projection operators are in accordance with the physics of the problem at hand.

7 Acknowledgment

The authors are thankful to Prof. Beirão da Veiga for the theoretical support in modelling permanent magnets in the Kikuchi formulation. Moreover, Franco Dassi was partially supported by the European Research Council through the H2020 Consolidator Grant (grant no. 681162) CAVE – Challenges and Advancements in Virtual Elements.

8 References

[1] da Veiga, L.B., Dassi, F., Russo, A.: 'High-order virtual element method on polyhedral meshes', *Comput. Math. Appl.*, 2017, **74**, (5), pp. 1110–1122. Available at: https://doi.org/10.1016/j.camwa.2017.03.021

[2] da Veiga, L.B., Russo, A., Vacca, G.: 'The virtual element method with curved edges', *ESAIM: Math. Model. Numer. Anal.*, 2019, **53**, (2), pp. 375–404. Available at: https://doi.org/10.1051/m2an/2018052

[3] Dassi, F., Fumagalli, A., Losapio, D., *et al.*: 'The mixed virtual element method on curved edges in two dimensions', 2020. arXiv:2007.13513

[4] Beirão.da Veiga, L., Brezzi, F., Cangiani, A., *et al.*: 'Basic principles of virtual element methods', *Math. Models Methods Appl. Sci.*, 2013, **23**, (1), pp. 199–214

[5] Vacca, G.: 'An H^1at-conforming virtual element for Darcy and Brinkman equations', *Math. Models Methods Appl. Sci.*, 2017, **28**, (1), pp. 159–194. Available at: https://doi.org/10.1142/s0218202518500057

[6] da Veiga, L.B., Lovadina, C., Vacca, G.: 'Virtual elements for the Navier–Stokes problem on polygonal meshes', *SIAM J. Numer. Anal.*, 2018, **56**, (3), pp. 1210–1242. Available at: https://doi.org/10.1137/17m1132811

[7] Berrone, S., Borio, A., Vicini, F.: 'Reliable a posteriori mesh adaptivity in discrete fracture network flow simulations', *Comput. Methods Appl. Mech. Eng.*, 2019, **354**, pp. 904–931

[8] Mascotto, L.: 'Ill-conditioning in the virtual element method: stabilizations and bases', *Numer. Methods Partial Diff. Equ.*, 2018, **34**, (4), pp. 1258–1281

[9] Berrone, S., Borio, A., Pieraccini, S., *et al.*: 'New strategies for the simulation of the flow in three dimensional poro-fractured media'. European Conf. on Numerical Mathematics and Advanced Applications, Voss, Norway, 2017, pp. 715–723

[10] Ahmad, B., Alsaedi, A., Brezzi, F., *et al.*: 'Equivalent projectors for virtual element methods', *Comput. Math. Appl.*, 2013, **66**, (3), pp. 376–391

[11] Kikuchi, F.: 'Mixed formulations for finite element analysis of magnetostatic and electrostatic problems', *Jpn. J. Appl. Math.*, 1989, **6**, pp. 209–221

[12] Reece, A.B.J., Preston, T.W.: '*Finite element methods in electrical power engineering*' (Courier Corporation, USA, 2000)

[13] da Veiga, L.B., Brezzi, F., Dassi, F., *et al.*: 'Virtual element approximation of 2d magnetostatic problems', *Comput. Methods Appl. Mech. Eng.*, 2017, **327**, pp. 173–195. Advances in Computational Mechanics and Scientific Computation-the Cutting Edge. Available at: http://www.sciencedirect.com/science/article/pii/S0045782517305935

[14] Di Barba, P., Savini, A., Wiak, S.: '*Field models in electricity and magnetism*' (Springer Science & Business Media, USA, 2008)

[15] Mentor.Graphics, A.S.B.: 'Magnet, version 7.9'. Available at: https://www.mentor.com/products/mechanical/magnet/magnet/

[16] Bossavit, A.: '*Computational electromagnetism: variational formulations, complementarity, edge elements*' (Academic Press, USA, 1998)

[17] Di Barba, P., Marini, L.D., Savini, A.: 'Mixed finite elements in magnetostatics', *COMPEL – Int. J. Comput. Math. Electr. Electron. Eng.*, 1993, **12**, pp. 113–124

[18] Di Barba, P., Perugia, I., Savini, A.: 'Recent experiences on mixed finite elements for 2d simulations of magnetic fields', *COMPEL – Int. J. Comput. Math. Electr. Electron. Eng.*, 1998, **17**, pp. 674–681

[19] Silvester, P.P., Ferrari, R.L.: '*Finite elements for electrical engineers*' (Cambridge University Press, UK, 1996)

[20] Bermúdez, A., Rodríguez, A., Villar, I.: 'Extended formulas to compute resultant and contact electromagnetic force and torque from Maxwell stress tensors', *IEEE Trans. Magn.*, 2016, **53**, (4), pp. 1–9

[21] Bianchi, N.: '*Electrical machine analysis using finite elements*' (CRC Press, USA, 2017)

[22] Maday, Y., Mavriplis, C., Patera, A.: '*Nonconforming mortar element methods: application to spectral discretizations*' (NASA Technical Reports Server, USA, 1988)

[23] Buffa, A., Maday, Y., Rapetti, F.: 'A sliding mesh-mortar method for a two dimensional eddy currents model of electric engines', *ESAIM: Math. Model. Numer. Anal.-Modélisation Mathématique et Analyse Numérique*, 2001, **35**, (2), pp. 191–228